ASME Journal of Manufacturing Science and Engineering
Online journal at:
https://asmedigitalcollection.asme.org/manufacturingscience

Kijoon Lee[1]
School of Mechanical, Industrial, and Manufacturing Engineering, Oregon State University, Corvallis, OR 97331; Advanced Technology and Manufacturing Institute (ATAMI), Corvallis, OR 97330
e-mail: leekij@oregonstate.edu

Milad Ghayoor
School of Mechanical, Industrial, and Manufacturing Engineering, Oregon State University, Corvallis, OR 97331; Advanced Technology and Manufacturing Institute (ATAMI), Corvallis, OR 97330
e-mail: milad.ghayoor@smith-nephew.com

V. Vinay K. Doddapaneni
School of Chemical, Biological, and Environmental Engineering, Oregon State University, Corvallis, OR 97331
e-mail: doddapav@oregonstate.edu

Kenta Noma
School of Mechanical, Industrial, and Manufacturing Engineering, Oregon State University, Corvallis, OR 97331
e-mail: kenta.noma13@gmail.com

Somayeh Pasebani
School of Mechanical, Industrial, and Manufacturing Engineering, Oregon State University, Corvallis, OR 97331; Advanced Technology and Manufacturing Institute (ATAMI), Corvallis, OR 97330
e-mail: somayeh.pasebani@oregonstate.edu

Chih-Hung Chang
School of Chemical, Biological, and Environmental Engineering, Oregon State University, Corvallis, OR 97331
e-mail: chih-hung.chang@oregonstate.edu

A Microchannel Heat Exchanger Produced From a Metal Matrix Composite by Hybrid Laser Powder Bed Fusion and Inkjet Printing

This paper explores the production of an oxide dispersion strengthened (ODS) 304L stainless steel microchannel heat exchanger (HX) using a hybrid additive manufacturing process of laser powder bed fusion and inkjet printing. The study investigates the capabilities and economics of the hybrid inkjet-laser powder bed fusion (LPBF) process and evaluates the dimensional accuracy, functionality, and mechanical properties of the resulting ODS alloy. The effectiveness and pressure drop of the ODS heat exchangers produced by the hybrid LPBF tool are also determined. Results show that the inkjet-doped samples have a lower mean channel height with higher standard deviation than samples produced by LPBF alone. This is attributed to greater absorption of laser energy for the powder coated with the oxide precursor. The economic analysis shows that the hybrid process has a potential for reducing the unit cost of the heat exchanger based on cost modeling assumptions. [DOI: 10.1115/1.4065820]

Keywords: laser powder bed fusion, metal matrix composite, stainless steel

[1]Corresponding author.
Manuscript received August 26, 2023; final manuscript received June 17, 2024; published online July 15, 2024. Assoc. Editor: Kevin Chou.

Brian Fronk
School of Mechanical, Industrial,
and Manufacturing Engineering,
Oregon State University,
Corvallis, OR 97331
e-mail: bmf141@psu.edu

Brian K. Paul
School of Mechanical, Industrial,
and Manufacturing Engineering,
Oregon State University,
Corvallis, OR 97331;
Advanced Technology
and Manufacturing Institute (ATAMI),
Corvallis, OR 97330
e-mail: brian.paul@oregonstate.edu

1 Introduction

Around 50% of the global demand for hydrogen is met by steam methane reforming [1], in which steam and methane react at high temperatures (~800 °C) to produce hydrogen gas (H_2) and carbon byproducts. To increase system efficiency, waste heat in the reaction stream can be recuperated to heat the incoming steam and methane, reducing the amount of heat required for reaction [2]. The cost of high-temperature recuperative heat exchangers (HXs) needed to recuperate this high-grade waste heat is dominated by the cost of the raw material, typically a Ni-based superalloy. Therefore, one strategy to reduce the cost of these high-temperature recuperators has been by using microchannels, characterized by dimensions below 1 mm, resulting in laminar flow conditions capable of supporting higher heat transfer rates, shorter flow paths, and higher surface area per unit volume [3].

Due to the effects of flow maldistribution, the heat transfer performance of microchannel heat exchangers (MCHXs) can be affected by tolerances above 5% of channel height [4]. Typically, MCHXs are produced as-printed circuit heat exchangers (PCHEs) by diffusion bonding a stack of laminae with photochemically-machined patterns of channels and headers. PCHEs made out of Ni-based superalloys are expensive to produce driven by poor material utilization during the photochemical machining step [5], which could hinder their commercial adoption.

In the past, to lower manufacturing costs, metal matrix composites, in the form of oxide-dispersion-strengthened (ODS) austenitic SS composites, have been pursued as a potentially cheaper alternative to Ni-based superalloys owing to the low cost of the iron-based alloy. The high-temperature stability and creep resistance of these materials can be on par with those of Ni-based superalloys and are a function of oxide nanoparticle dispersants within the metal matrix, which can sit on grain boundaries, pinning them to avert grain coarsening [6].

However, these wrought ODS alloys possess anisotropic mechanical properties caused by the elongation of grains during extrusion processes [7]. Further, the conventional manufacturing of ODS alloys in wrought forms involves solid-state production techniques, making them too expensive to employ through conventional PCHE routes [8]. Zhang and Gümmer [9] provided a summary of several commonly considered candidate materials for high-temperature HX, focusing on material costs. Their analysis revealed that the material cost of ODS PM 2000 is approximately up to ten times higher than that of SS, while Inconel 625 is about 4–5 times more expensive than SS. To avert the cost of the conventional multi-step solid-state process, Maier et al. [10] fabricated an ODS alloy tube using cold spray processes. Pre-alloyed 14YWT (Fe-14%Cr, 3%W, 0.4%Ti, 0.2%Y, 0.01%O) powders were sprayed and deposited on a rotating aluminum alloy tube using nitrogen gas. After surface polishing of the deposit to the desired cladding thickness, the aluminum alloy was dissolved in an alkaline medium leaving a free-standing ODS tube. More recently, metal additive manufacturing (AM) technologies have been applied to produce the ODS alloy. Yang [11] examined the microstructure and mechanical properties of austenitic ODS 316L SS produced via directed energy deposition (DED) using gas-atomized 316L SS powder with 0.14 wt% yttrium oxide. The study evaluated the thermal stability of DED-produced ODS steels. Post 100-h exposure at 1000 °C in argon, a partially recrystallized microstructure with fewer crystalline Y-O-enriched nanoparticles emerged. The post-heat treatment samples exhibited a lower tensile strength of 592 MPa but higher elongation of 42% compared to the as-printed samples. Moreover, Wilms et al. [12] demonstrated the successful fabrication of an iron-based ODS PM2000 composite ($Fe20Cr4.5Al0.5Ti + 0.5Y_2O_3$ in wt%) using high-speed laser cladding in the DED process. Key achievements include the effective dispersion of nano-scaled yttrium-based oxides in the ferritic SS matrix, overcoming common nanoparticle agglomeration issues seen in conventional DED processes. This resulted in smaller dispersoid sizes and increased hardness of the specimen compared to those manufactured by standard DED. However, this approach is limited in its ability to produce complex geometries with small dimensions.

In contrast, among AM processes, laser powder bed fusion (LPBF) stands out as the most suitable technique for fabricating functional devices, such as MCHX with complex internal geometries. This is because LPBF offers superior feature resolution and accuracy compared to other metal AM processes [13–15]. Furthermore, LPBF has begun to be used to produce MCHXs for specialty markets due to higher material utilization and greater accessibility within the supply chain through AM service bureaus [16].

More recently, ODS alloys have been produced by LPBF as shown in Fig. 1(*a*) using mechanical alloying powder [17,18], providing a means toward implementing more complex geometries with refined dimensions. Ghayoor et al. [19] successfully produced a nearly fully dense austenitic ODS 304L SS alloy using a process that involved light ball-milling followed by LPBF. Additionally, they explored the impact of yttria particle addition on the mechanical properties of the alloy at room temperature. In a subsequent study, Ghayoor et al. [20] conducted a detailed investigation into the thermal stability of yttrium oxide nanoparticles in the ODS 304L alloy under high-temperature aging treatment. Moreover, they evaluated the high-temperature mechanical properties and creep resistance of the ball-milled LPBF 304L ODS alloy. However, scaling up these processes presents challenges, as the ball-milling required for pre-mixing stainless steel and oxide powders is tedious, costly, and time-consuming.

Recently, research efforts have focused on alternatives to mechanical alloying. Horn et al. [21] investigated the use of gas

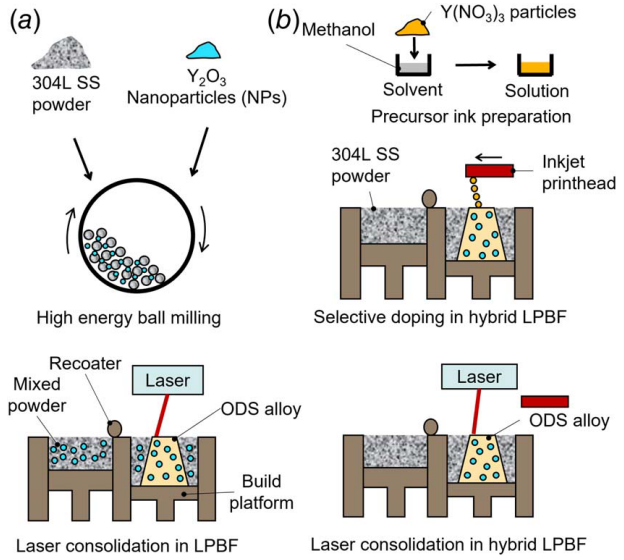

Fig. 1 Schematic diagram of (*a*) ODS fabrication by light ball-milling followed by LPBF and (*b*) ODS fabrication using hybrid inkjet-LPBF

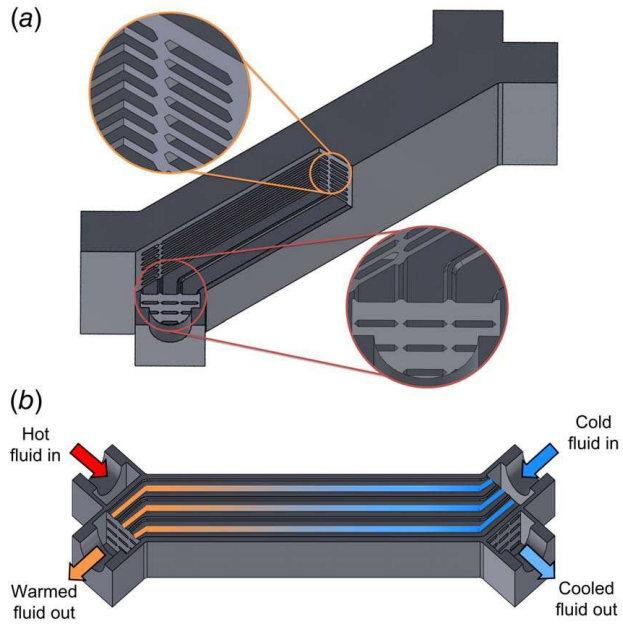

Fig. 2 MCHX design: section view showing (*a*) microchannels in the body and inlet and (*b*) cold-side channel

atomization reaction synthesis (GARS) steel powders, comprising 15 wt% Cr with minor alloying elements of 0.15 wt% Y and 0.10% Ti, to eliminate the need for pre-alloying powder. Analysis of the LPBF-fabricated solids showed a substantial presence of nano-scale Y-Ti oxides in the microstructures, derived from the GARS precursor powders. Although an in-depth microstructural analysis was conducted, mechanical property evaluations, such as tensile testing at room or elevated temperatures, were not included in this study.

In 2020, Paul et al. [22,23] reported a method for scaling the production of ODS composites using LPBF by doping powder beds with oxide precursors, via a piezo-electric inkjet printhead (Xerox M series) within a 3D Systems ProX DMP 300 machine, prior to laser consolidation (Fig. 1(*b*)). This innovative approach eliminates the need for ball-milling by introducing the oxide particles during the LPBF process, thereby resolving the issue of scalability. ODS 316L SS [24] was created by applying an ethanol-based ink with Al_{13} nanoclusters (NCs) onto 316L SS powder, followed by laser processing. Additionally, a 316L SS-Cu metal matrix composite was developed to increase effective thermal conductivity compared to 316L SS, employing a jettable Cu ink and emulating the hybrid LPBF-inkjet method [25,26].

To the best of the author's knowledge, while numerous papers have focused on the microstructural and mechanical analyses of simple-shaped test coupons made of ODS alloys using LPBF or DED, there is a lack of research on the fabrication and evaluation of high-temperature HXs made of ODS alloy produced using LPBF. Therefore, the objective of this paper is twofold: (1) to evaluate the high-temperature yield strength (YS) of the new ODS material made using the hybrid process in comparison with 304 stainless steel; and (2) to investigate the use of the new method to produce a simple HX using the new material. This study delves into the capabilities and economic viability of the hybrid LPBF-inkjet process specifically for fabricating an MCHX using an ODS 304L SS composite. Device testing is used as a means to evaluate the effectiveness of the new process for producing a geometry of interest as well as determining which geometric parameters are most in need of improving for future application. The dimensional accuracy of the heat exchanger is explored.

2 Experimental Methods

2.1 Heat Exchanger Fabrication. Figure 2(*a*) is a rendering of the MCHX showing an array of microchannels with alternating hot and cold fluid in the vertical direction. Figure 2(*b*) shows an incoming cold feedstock gas flowing through the cold-side channels to an outlet where it has been heated. In contrast, the incoming hot gas flows in the opposite direction in the layer below, eventually leaving at a cooler temperature. A specification of the dimensions within the MCHX is shown in Table 1. Figure 3 shows the inkjet module integrated with the 3D systems LPBF machine. Additionally, Fig. 4 shows a process block diagram for producing an ODS 304L MCHX using the hybrid LPBF-inkjet method. During the hybrid LPBF process, four steps were repeated prior to removal from the LPBF tool. First, metal powder was layered, and then the laser was used to melt the metallic powder particles and oxide nanoparticles, and convectively mix the constituents, followed by oxide precipitation upon solidification and remelting. Afterward, the precursor ink was jetted onto the consolidated metal using the inkjet printhead. Finally, the laser was scanned over to evaporate the solvent out of the ink and convert the precursor into yttrium oxide. The next step involved removing the unused powder from the build plate. Then, the build plate, including the printed part, was taken out from the machine tool, and detached from the build plate and the support structures using wire electrical discharge machining (EDM). Finally, the detached part and build plate were ground by hand to remove any remaining support structure. In this study, two types of HXs were fabricated. The first type, made of 304L SS, is denoted as 304 HX (44/na/5 deg). The other three, made of ODS 304L SS using a hybrid LPBF-inkjet technique, are labeled as follows: (1) ODS HX (58/29/5 deg); (2) ODS HX (44/29/5 deg); and (3) ODS HX (44/29/30 deg). The labels indicate the laser volumetric energy density (VED) values used for consolidation and ink conversion, along with the build orientation. For

Table 1 Specifications of the MCHX test article produced in this work

Parameters	Hot side	Cold side	Both
Channel height	762 μm	635 μm	—
Channel width	—	—	5.1 mm
Channel length	—	—	94.5 mm
Number of channels	24 ea	21 ea	—
HX volume	—	—	28,557 mm^3
HX surface area	—	—	59,665 mm^2

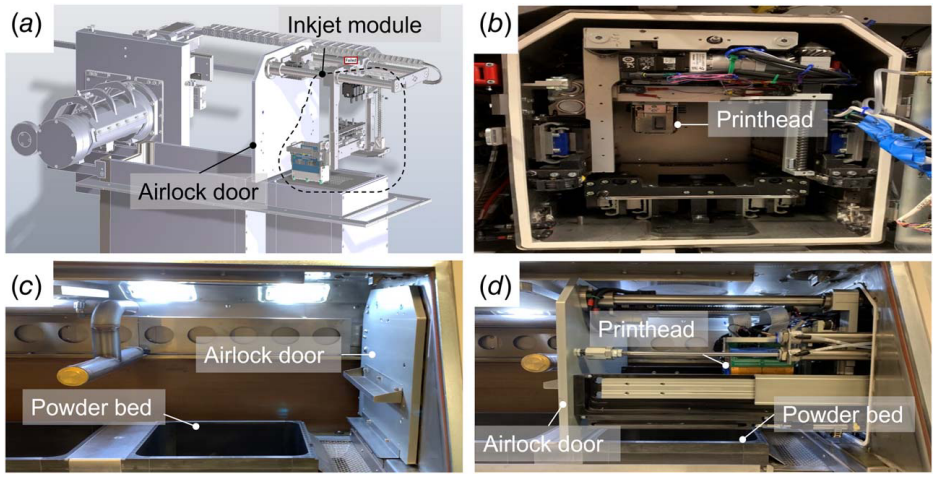

Fig. 3 (*a*) Solid model of hybrid system, (*b*) end view of airlock showing installed Xerox module, (*c*) before, and (*d*) after Xerox module extending over powder bed chamber, (reproduced with permission from Ref. [22])

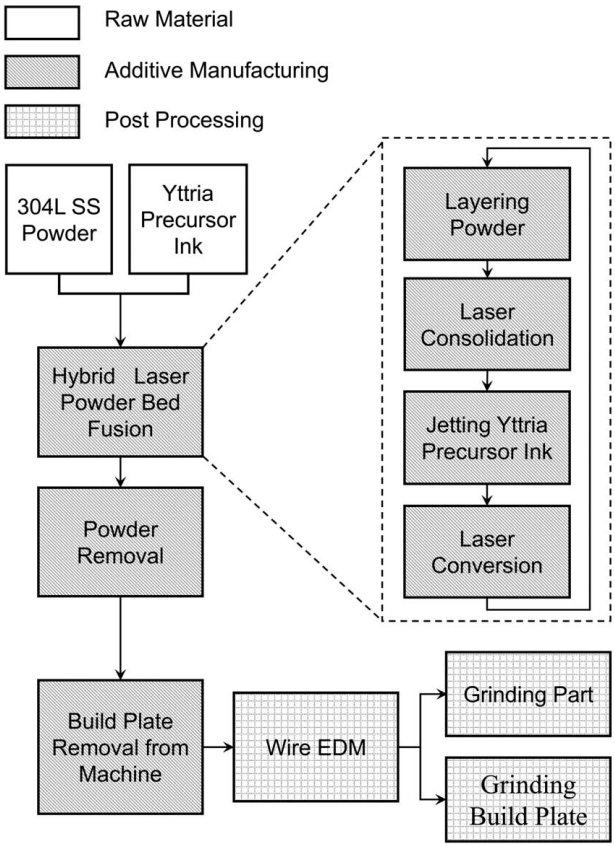

Fig. 4 Process block diagram for hybrid LPBF ODS 304L MCHX

instance, the label ODS HX (58/29/5 deg) represents the process parameters for this HX, specifying 58 J/mm^3 and 29 J/mm^3 as the laser VEDs, and 5 deg as the build orientation.

2.1.1 Materials. Sandvik Osprey gas-atomized AISI 304L austenitic SS powder was characterized by dynamic light scattering, showing a powder distribution of D10 = 23 μm, D50 = 33 μm, and D90 = 44 μm. To produce the precursor ink, yttrium nitrate hexahydrate, 99.8% $Y(NO_3)_3$ (Sigma-Aldrich Inc., St. Louis, MO) was dissolved in methanol (CH_3OH) with a concentration of 1.83 mol/l. The thermal decomposition of the ink is described as follows [27]:

$$4Y(NO_3)_3 \cdot 6H_2O = 2Y_2O_3 + 6N_2O_5 + 24H_2O \quad (1)$$

In prior work, X-ray diffraction was performed to confirm laser conversion of the precursor and the required amount of jetted ink was calibrated to deposit 0.5 wt% yttria in 304L SS metal matrix [22].

2.1.2 Laser Powder Bed Fusion. Table 2 shows the process parameters used for producing the ODS 304 MCHXs and 304L SS MCHX. To produce the ODS MCHXs using the hybrid LPBF method, the laser was scanned twice per layer to ensure the solvent was fully evaporated prior to consolidation. The precursor ink was jetted on the metal substrate, followed by laser irradiation for driving off the solvent and thermal decomposition of precursor. Then, metal powder was layered on top and a final laser scan was used for melting powder, converting oxide, and convective mixing. The mean laser VED was calculated as Eq. (2).

$$\text{VED} = \frac{P}{v \times hs \times t} \quad (2)$$

where P is the laser power, v is the scan speed, hs is the hatching space, and t is the layer thickness.

2.2 Materials Testing. Once the HXs were produced, tensile bars of the ODS alloy were separately built parallel to the surface of the build plate using hybrid inkjet-LPBF tool and the precursor ink. Following the ASTM E8 standard, the tensile bars had a thickness of 1.0 mm and a gauge width and length of 6.25 mm and 25 mm, respectively. Tensile properties were measured at 600 °C on an Instron 5969 universal tester equipped with an Instron furnace with a soaking time of 10 min. The VEDs used for fabricating tensile bars were 44 J/mm^3 and 29 J/mm^3 for consolidation and conversion step, respectively.

2.3 Heat Exchanger Testing. Device testing was conducted to evaluate the dimensional capability of the new hybrid LPBF method for producing an HX geometry. Before testing the devices, a thorough depowdering process was implemented to ensure that the pressure drop values were not affected by unused powder remaining in the microchannels. This process began after the HXs were detached from the build plate using wire EDM. The depowdering procedure was as follows: each HX was submerged in de-ionized water in an ultrasonic container and ultrasonicated for 5 min. Afterward, pressurized air was used to clear the

Table 2 Process parameters for hybrid LPBF processes for ODS 304L SS MCHXs and 304L SS MCHX

HX name	Process	Mean VED (J/mm^3)	Beam power (W)	Scanning speed (mm/s)	Hatching space (mm)	Layer thickness (mm)	Build orientation (deg)
ODS HX (58/29/5)	Consolidation	58	175	1000	0.075	0.040	5
	Conversion	29	175	2000	0.075	0.040	
ODS HX (44/29/5)	Consolidation	44	175	2000	0.050	0.040	5
	Conversion	29	175	2000	0.075	0.040	
ODS HX (44/29/30)	Consolidation	44	175	2000	0.050	0.040	30
	Conversion	29	175	2000	0.075	0.040	
304 HX (44/na/5)	Consolidation	44	175	2000	0.050	0.040	5
	Conversion	n/a	n/a	n/a	n/a	n/a	n/a

Note: The parameters in parentheses along the *x*-axis are (consolidation VED/conversion VED/build orientation).

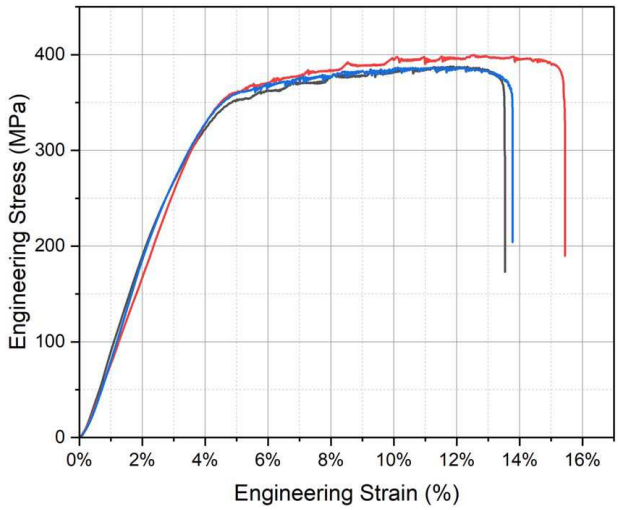

Fig. 5 Stress–strain curves for hybrid LPBF ODS 304L SS specimens at 600 °C

microchannels, effectively removing any trapped powder from the complex channels. This process was repeated for each HX until no residual powder was released from the device. Once depowdering was complete, each HX was inserted into a test loop to evaluate thermal and pressure drop performance. The compressed air as the working fluid was supplied through a flowmeter to the cold channel inlet of the HX. For effectiveness testing, the air flow rates were controlled and maintained at 1, 2, and 3 g/s. The air leaving the cold outlet was heated by passing through a tube heater, and flowed in the hot side channel by exchanging the heat with the cold air. The cooled air exited to the atmosphere. The temperatures were measured using K-type thermocouples at the inlet and outlet of both sides. For pressure drop testing, the pressure drops at both channels were obtained by measuring the pressures at the inlet and exit pressures at both sides using pressure transducers. Subsequently, the measured pressures were compared with two theoretical pressure drop values. These comparisons aimed to evaluate the dimensional capability of the hybrid process in producing a functional HX. The first comparison was performed by using theoretical pressure drops calculated from the nominal ideal channel dimensions of the HX, as described in Table 1. An additional comparison was also made to determine whether significant channel blockage occurred due to unused powder trapped in the microchannel. For this, the pressure drops were predicted based on the actual channel dimensions and the characterized surface roughness. Two distinct equations, Eq. (A9) for the first comparison and Eq. (A11) for the second comparison, were employed to calculate two separate friction factors. These equations are available in Appendix.

2.4 Characterizing Channel Dimensions. After HX testing, the size of the microchannels within the HX was characterized by cross-sectioning the HXs perpendicular to the fluid direction using wire EDM. Next, the cross-sectional images of both hot and cold channels were obtained using an optical microscope. These images were then imported into IMAGEJ software and converted to black and white images for enhancing the accuracy of height measurement. Then the average heights of the hot and cold channels were measured using IMAGEJ to measure over eight locations from each of the eight cross sections. The surface roughness values were derived from the measured heights obtained with IMAGEJ. These roughness values were calculated by dividing the sum of the absolute values of the height deviations from the mean line by the number of measurements for each HX.

3 Results and Discussion

3.1 Mechanical Properties at High Temperature. Figure 5 displays three stress–strain curves tested at 600 °C for the hybrid LPBF ODS 304L SS specimens produced under the identical

Table 3 A comparison of yield strength (MPa) and ultimate tensile strength (MPa) of ODS alloy at different temperatures

Material	YS at RT	UTS at RT	YS at 600 °C	UTS at 600 °C	YS at 700 °C	UTS at 700 °C
Hybrid LPBF ODS 304L (this paper)	586 ± 9 [22]	695 ± 9 [22]	313 ± 20	392 ± 6	—	—
LPBF ODS 304L [20]	575 ± 8	700 ± 13	290 ± 2	370 ± 4	217 ± 1	229 ± 1
Annealed 304 [28]	290	579	113	367	95	241
HIP ODS 304 [29]	—	—	—	410	—	300
HIP ODS 304 [30]	525	940	—	—	—	415
HIP + Forging ODS 304 [30]	595	925	—	—	—	395
LENS[a] ODS Fe-Cr [31]	—	794	—	461	—	—
HIP LENS ODS Fe-Cr [31]	—	1046	—	592	—	—
LPBF Inconel 625 [32]	770	1039	570	881	—	—
HIP LPBF Inconel 625 [33]	459.5 ± 6.5	926.0 ± 12.7	246.2 ± 4 (at 650 °C)	637.5 ± 15 (at 650 °C)	—	—

[a]LENS: laser-engineered net shaping.

Table 4 A comparison of elongation of ODS alloy at different temperatures

Material	Elongation (%) at RT	Elongation (%) at 600 °C	Elongation (%) at 700 °C
Hybrid LPBF ODS 304L (this paper)	51 ± 3 [22]	14 ± 1	—
LPBF ODS 304L [20]	32 ± 5	23 ± 1	21.5 ± 1
Annealed 304 [28]	55	35	35
HIP ODS 304 [29]	—	—	—
HIP ODS 304 [30]	24.5	—	12
HIP + Forging ODS 304 [30]	43.5	—	17.5
LENS ODS Fe-Cr [31]	5.0	4.0	—
HIP LENS ODS Fe-Cr [31]	7.7	10.3	—
LPBF Inconel 625 [32]	40	32	20
HIP LPBF Inconel 625 [33]	74.9 ± 3	38.7 ± 5	—

conditions described in Sec. 2.2. Three tensile tests were conducted to determine the average and standard deviation. The value of YS, ultimate tensile strength (UTS), and elongation of these specimens at 600 °C was found to be 313 ± 20 MPa, 392 ± 6 MPa, and 14 ± 1%, respectively. Tables 3 and 4 compare the tensile properties of the ODS 304L composite produced in this work using hybrid LPBF with those of previously published austenitic ODS composites, such as ODS 304L [20] and ODS 304 composite [29,30]. The yield strength and ultimate tensile strength of the ODS alloy produced in this work at room temperature and 600 °C were found to be similar to the values of LPBF ODS 304L composite [20] produced by pre-mixing 304L SS powder with yttria nanoparticles via ball-milling, followed by consolidation via LPBF. This is likely due to the microstructures with precipitations identified as Y–Si–O compounds, which are similar to those produced by ball-milling followed by LPBF, as indicated in prior work [22]. It is important to note that previous research [22] found that jetting dopant ink onto the powder bed led to microstructural defects, such as spherical shapes and small-sized pores. This occurred because the solvent did not fully evaporate from the bed before consolidation, owing to the high surface energy in the bed. To resolve this issue, the process steps, as illustrated in Fig. 4, were modified to include additional laser irradiation. This extra step of laser irradiation enabled us to not only remove residual solvent but also fully decompose the precursor into yttrium oxide before consolidation. This effectively eliminated the pores caused by the flash evaporation of the solvent and gas byproducts.

However, the ductility of hybrid LPBF ODS was found to be low than that of previously published ODS alloys, likely due to the coarse oxide agglomeration intermittently observed in the cross-sectional microstructures. Prior research [22] that produced ODS 304L SS via hybrid LPBF showed a microstructure characterized by well-distributed nano-sized spherical precipitates, along with yttrium oxide agglomeration. Prior microstructure-based representative volume element simulations, as conducted by Ma and Wang [34], revealed that initial damage occurs in the Al_3Ti agglomeration under relatively small strain within the composite. Furthermore, Sun et al. [35] found that an increase in the agglomerated ratio expedites the stress concentration. Given these findings, it is expected that at an elevated temperature of 600 °C, the discrepancy in the coefficient of thermal expansion between the oxide agglomeration and the iron-based matrix results in void formation, thereby accelerating crack propagation and leading to a reduction in elongation.

3.2 Heat Exchanger Performance. Figure 6 shows the experimental and theoretically-calculated HX effectiveness. Both experimental and estimated values decrease as the mass flow rate increases. Also, the difference between the experimental and theoretical values decreases as the mass flow rate increases. This could be due to more heat loss to ambient at a lower mass flow rate.

Figures 7(*a*) and 7(*b*) show the total pressure drop values with polynomial fit curves for the cold side and the hot side of the HXs along with the theoretical pressure drop values calculated

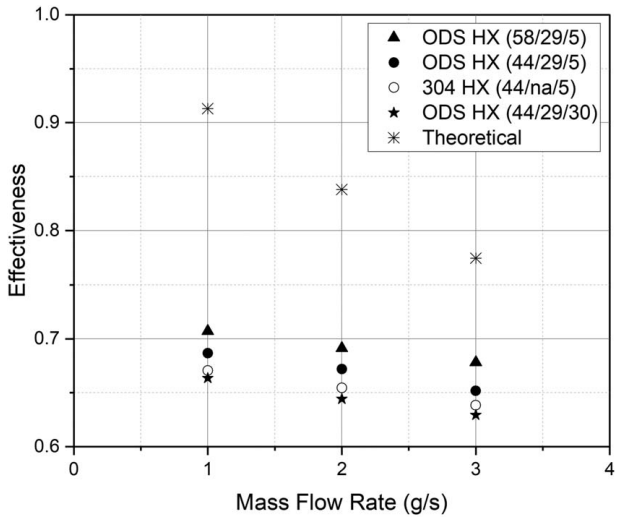

Fig. 6 Comparison of experimental and theoretical effectiveness as a function of mass flow rate

based on the nominal channel dimensions, as depicted in Table 1. As shown, the experimental pressure drops increase with the square of the mass flow rate, whereas the theoretical values increase linearly with the mass flow rate. This is due to the roughened conditions of the actual printed channel walls which likely depart from pipe flow assumptions used in the calculations that do not account for the impact of roughness. Moreover, the flow characteristics in microchannels can be deviant from the conventional flow theories. The previous research [36] on heat transfer and fluid flow patterns in rectangular microchannels indicated that the friction factor was greater than what conventional theory had previously suggested. Their experimental data demonstrated that the shift from laminar to turbulent flow happens at the Reynolds number ranging from 300 to 900. In addition, according to the previous research [37], as the Reynolds number increases in the turbulent regime, the thickness of the laminar sublayer decreases, and the roughness of the inner pipe surface becomes important. Therefore, a more rigorous analysis of the pressure drops in the channels was conducted. Additional theoretical values were derived, utilizing the actual channel dimensions and taking into account the effects of roughness. These revised values were then compared with the actual measurements, as illustrated in Fig. 8.

Additionally, the results of effectiveness and pressure drops presented in Figs. 6–8 are discussed in more detail in the subsequent section, following the discussion of the measured channel dimensions.

3.3 Channel Dimensions. To better understand the heat exchanger performance, efforts were made to characterize the

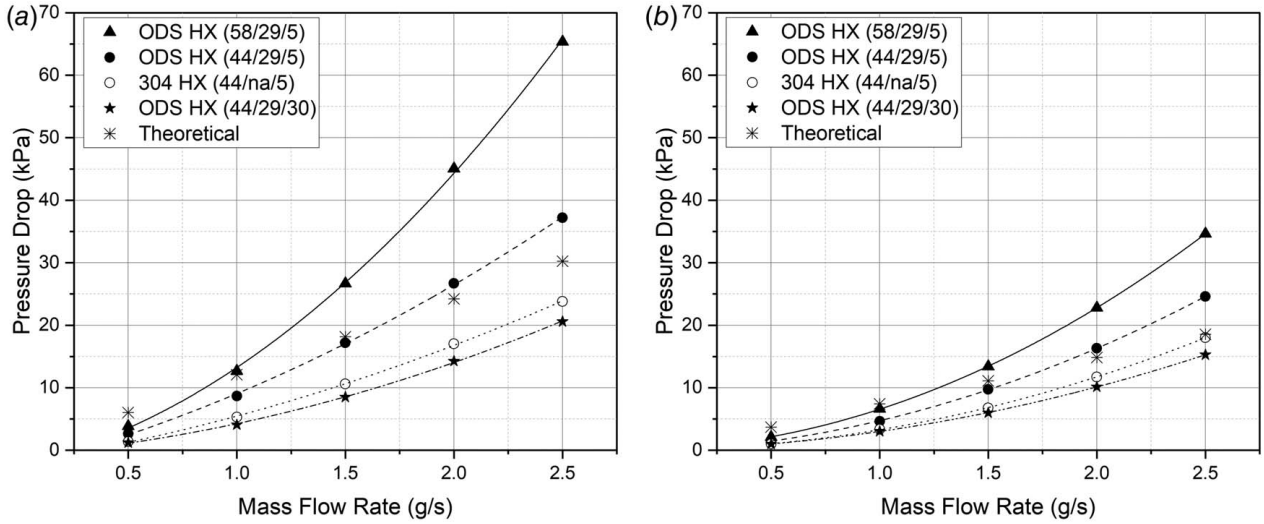

Fig. 7 Comparison of experimental and theoretical pressure drops in (*a*) cold side and (*b*) hot side channels, based on nominal channel sizes, across various mass flow rates

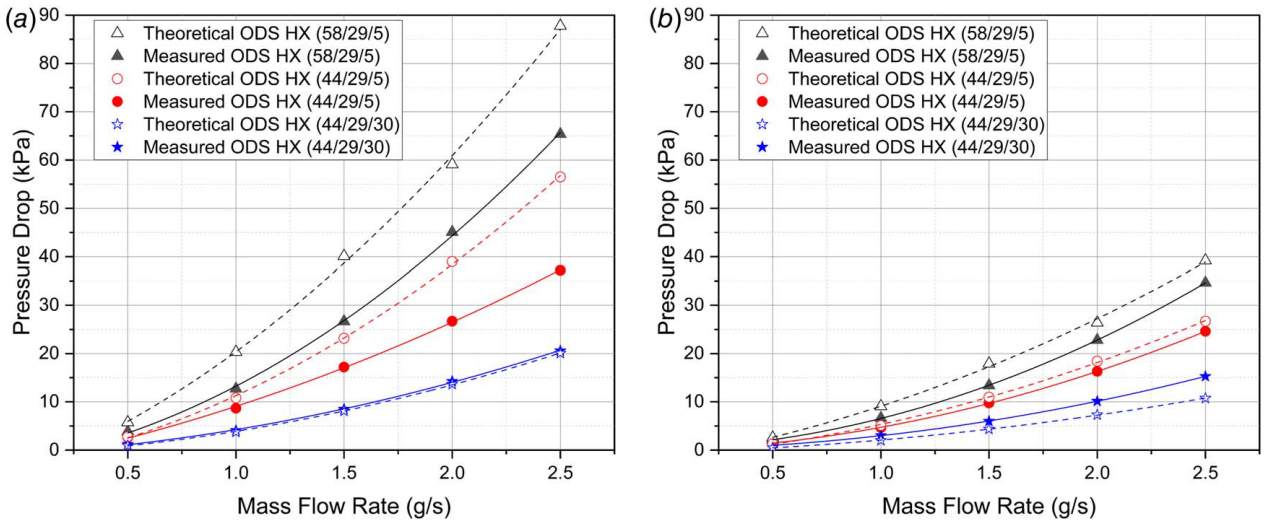

Fig. 8 Comparison of experimental and theoretical pressure drops in (*a*) cold side and (*b*) hot side channels, based on actual channel dimensions and roughness, as a function of mass flow rates

height of the channels, which has a significant impact on both HX pressure drop and effectiveness. Figure 9 shows some of the cross sections used for investigating channel height. To enhance measurement accuracy, images captured through the optical microscope were transformed into a black and white format using IMAGEJ software. The black regions in the images signify the consolidated channel walls, while the white regions correspond to the fluid channels.

A summary of the results from optical microscopy of the channel heights is shown in Fig. 10. One finding is that higher VED made the mean channel height smaller due to the existence of larger weld pools. Moreover, increasing the build orientation increased the mean channel height, while reducing the standard deviation of the channel height.

The pressure drop and effectiveness of this condition (44/29/30 deg) were found to be the lowest among the four HXs due to the consequent larger channel sizes. When it comes to comparison among experimental effectiveness in Fig. 6, it was found that ODS HX (58/29/5 deg) and ODS HX (44/29/30 deg) have the highest and lowest values at all flow rates, respectively. The effectiveness of HX highly depends on the heat transfer within the channels, which is known to increase with decreasing channel size.

Further, concerning the pressure drop illustrated in Fig. 7, the experimental results show that higher VEDs lead to higher pressure drop. This is simply due to the smaller channel sizes at higher VED as shown previously. Moreover, it was observed that increasing the build orientation from 5 deg to 30 deg significantly reduced the pressure drop at all mass flow rates. This is attributed to the larger channel sizes and less standard deviation within the channels of the heat exchanger with the 30 deg orientation.

Figure 8 presents the additional comparison between the experimental and theoretical pressure drop values, which were calculated by considering the measured channel dimensions and roughness. The dashed lines represent the predicted values, while the solid lines denote the measured experimental values. Additionally, the same HXs are indicated by the same symbol. This comparison clearly demonstrates that the theoretical values align more accurately with the experimental ones compared to the previous comparison shown in Fig. 7. It was observed that the polynomial fit curves for all predicted values in Fig. 8, for both cold and hot side channels,

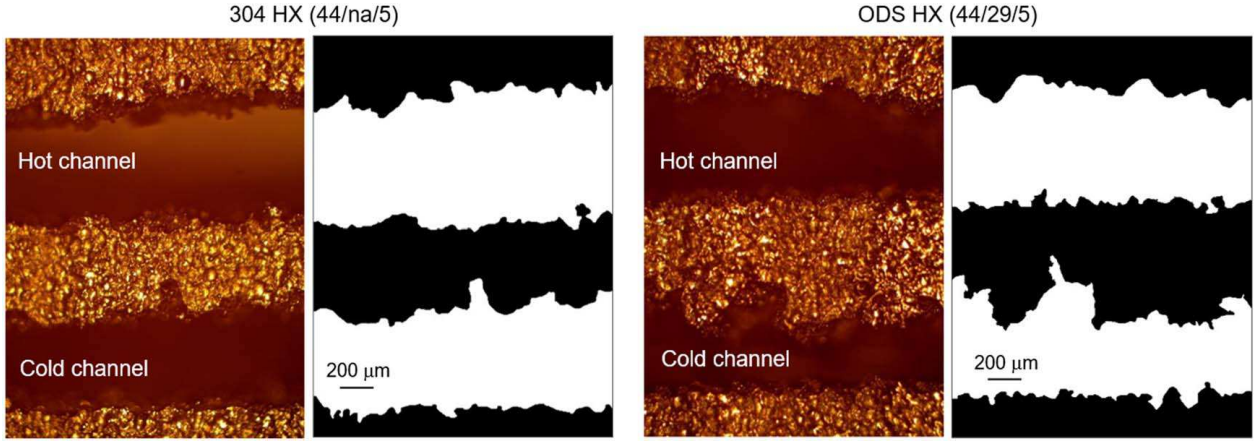

Fig. 9 Cross-sectional microchannels of (left) LPBF 304 HX and (right) LPBF-inkjet ODS HX

increase with the square of the mass flow rate, which is identical as those in the experimental values.

For both cold and hot side channels, the theoretical values for ODS HX (58/29/5 deg) and ODS HX (44/29/5 deg) overestimate, whereas those for ODS HX (44/29/30 deg) are almost identical to or slightly underestimate when compared to the experimental values. This reduction may be attributed to the fact that the surface roughness of the ODS HX (44/29/30 deg) is significantly lower than that of the other two HXs, with reductions of up to 58% and 39% for the cold and hot side channels, respectively, compared to the ODS HX (58/29/5 deg). Consequently, this diminishes the impact of roughness on pressure drops.

Based on the comparisons in Figs. 7 and 8, it can be concluded that the pressure drops primarily occurred due to smaller channels and high surface roughness within the channels. Moreover, while ODS HX (44/29/30 deg) exhibits slightly lower measured pressure drops compared to the theoretical values, the discrepancies are minor. This indicates that even if unused powder remains trapped in the microchannels, the quantity of residual powder is unlikely to significantly impact the usability of these HXs. Consequently, these HXs can still serve as effective tools for assessing the effectiveness of the hybrid LPBF process in creating a specific geometry and identifying which geometric parameters need enhancement for future applications.

More importantly, the observations regarding pressure drops and channel dimensions in ODS HXs emphasize the need to investigate the causes of channels with high surface roughness or size discrepancies. When comparing the pressure drop in the ODS HX (44/29/5 deg) with that in the 304 HX (44/na/5 deg), the channels created by inkjet technology were found to have higher pressure drop. Further comparison between the channel dimensions of the ODS HX (44/29/5 deg) and the 304 HX (44/na/5 deg) revealed that ink doping resulted in a reduced average channel size and an increased standard deviation. Given that the same process parameters were applied to both HXs, with the exception of ink doping and conversion, it is therefore deduced that the ink doping and/or conversion process is responsible for these differences.

Two hypotheses were investigated regarding the influence of ink doping and conversion on channel size. First, efforts were made to investigate whether additional heat was added by the heat of reaction during the ink conversion. The heat of reaction during ink conversion was calculated by deducting the standard enthalpy of formation of reactants from the heat of formation of products. Table 5 lists the standard heats of formation of $Y(NO_3)_3{\cdot}6H_2O$, Y_2O_3, N_2O_5, and H_2O. Based on the literature values in Table 5, the standard heat of reaction was calculated to be 1280.6 kJ/mol, indicating that the reaction was endothermic, not exothermic. This suggests that the heat of reaction was not a contributing factor in the reduction of the mean channel size. Additionally, to evaluate the potential impact of the endothermic reaction on the melt pool temperature, and subsequently, on the channel sizes, the heat of reaction per mol (1280.6 kJ/mol) during ink conversion was converted to the heat of reaction per volume, which was determined to be 0.6 J/mm^3. This value represents only about 1% of the laser energy density provided in this study. Therefore, we infer that the heat of reaction during the ink conversion is unlikely to have a significant effect on the channel sizes.

Consequently, a second hypothesis was formulated that the absorption of the laser energy was greater for the powder coated with the oxide precursor. To investigate the laser absorption, the reflectivity of a 304 SS substrate, with and without precursor, was measured three times using a Jasco UV/Vis/NIR spectrometer. Figure 11 shows the average reflectivity for each coupon. At a wavelength of 1070 nm (laser wavelength of the LPBF tool), the average reflectivity and standard deviation were found to be

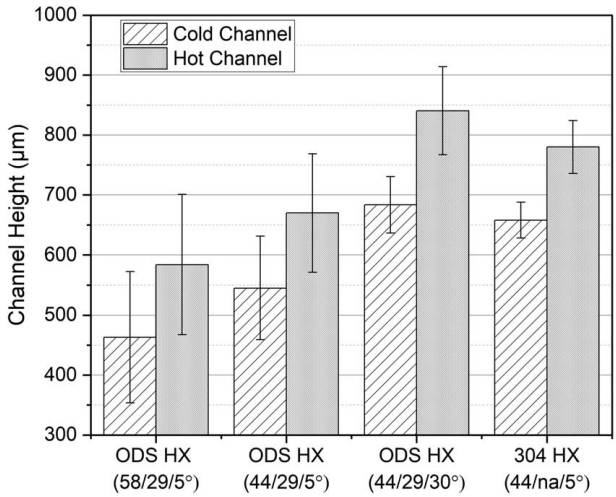

Fig. 10 Mean and standard deviation (error bar) of channel heights of heat exchangers

Table 5 Standard heats of formation

Chemical formula	Standard enthalpy of formation	References
$Y(NO_3)_3{\cdot}6H_2O$	−3043.9 kJ/mol	[38]
Y_2O_3	−1905.3 kJ/mol	[39]
N_2O_5	0.01 kJ/mol	[40]
H_2O	−241.8 kJ/mol	[40]

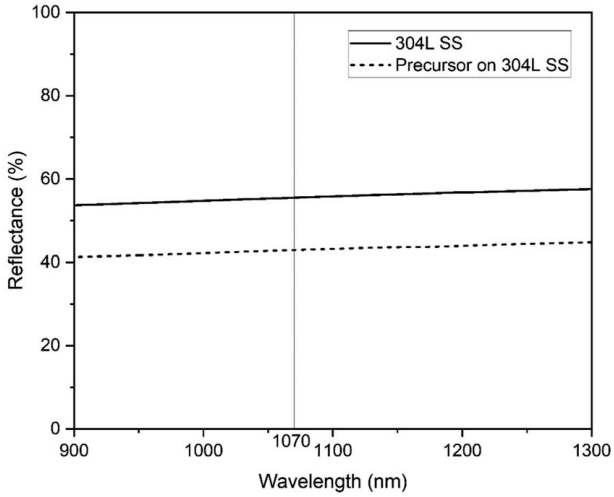

Fig. 11 Average reflectance with wavelength indicating that the 304L SS substrate with precursor absorbed more energy than 304L SS substrate alone

55.5% and 0.2%, respectively, for the 304L SS substrate. For the 304L SS substrate with precursor, the average reflectivity and standard deviation were 42.9% and 1.6%, respectively. These results suggest that the 304L SS substrate with precursor absorbed 28.3% more energy than the 304L SS substrate alone. This suggests that improved laser absorption caused by the doped ink led to larger weld pools and smaller channels. The findings of our study align with a previous study conducted by Ghayoor et al. [24], which indicated that the addition of Al_2O_3 NPs and Al_{13} NCs into 316L SS single tracks notably increased the depth of the melt pool.

4 Economic Analysis

To evaluate the economics of the hybrid LPBF-inkjet method, cost models were developed [41] and compared for both a same-sized Inconel 625 HX produced via LPBF and an ODS 304L HX produced via hybrid inkjet-LPBF. In the hybrid ODS 304L HX model, it was assumed that the laser was scanned once per layer, with a heated bed facilitating solvent evaporation. For this effort, the process flow for producing the Inconel 625 HX was identical to the process flow for the hybrid LPBF ODS HX with two exceptions: (1) Inc 625 powder was used instead of 304L SS powder and yttria precursor ink and (2) there is no jetting step in the LPBF cycle. Assumptions for the cost models are that capital investment is made for setting up a greenfield manufacturing plant. Thus, the cost models include cost recovery on capital equipment and facilities in addition to raw material, labor, maintenance, consumables, and utilities. Table 6 summarizes the assumptions used for both models. The detailed equations for this analysis can be found in Ref. [41].

Table 6 Assumptions used for both models

Parameter	Value
304L stainless steel powder cost (ODS HX)	\$47/kg
Yttrium nitrate hexahydrate cost (ODS HX)	\$700/kg
Methanol cost (ODS HX)	\$2.5/L
Inc 625 powder cost (Inc 625 HX)	\$165/kg
LPBF machine tool cost (Inc 625 HX)	\$808,565/tool
Hybrid LPBF machine tool cost (ODS HX)	\$908,565/tool
Equipment amortization schedule	10 year
Facility amortization schedule	30 year
Cost of manufacturing space	\$1000/m^2
Annual operator wages	\$50,000/year
Loaded labor cost rate	1.5 × wages
Operators required per tool	cycle time/ (load + unload time)
Total load and unload time	0.25 h
Annual maintenance	5% of capital cost
Electricity cost	\$0.0672/kWh
Process water cost	\$0.004/gal

4.1 Number of Parts Per Build. Maximizing the use of the work envelope in the LPBF process by printing multiple parts at a time can reduce the production cost of parts since layering time can be spread over multiple parts [42]. Yim and Rosen [43] presented an equation to calculate how many parts can fit to a work envelope considering the dimensions of a part and a work envelope, and the distances between parts. However, there are a few general rules of thumb for successful build in terms of positioning the parts in LPBF. This is because the build will likely fail if there are extreme contacts between the solidified parts and the recoating blade during powder layering. Moylan et al. [44] suggested the basic four guidelines to avoid extreme contact, each of which are depicted in Fig. 12.

First, a part should be rotated by a few degrees around the z-axis so the recoating blade does not pass over a long line of parallel contact with the part. Second, multiple parts need to be distributed to prevent simultaneous initial contacts with the recoating blade. Third, an overhang angle must not face into the recoating blade. Otherwise, a collision can result in deflecting the part upward, which can lead to delamination from the build plate. Fourth, the part cannot exceed a maximum vertical aspect ratio since the repeated contact can cause the part to bend.

Furthermore, especially for a heat exchanger that has internal channels, parts must be oriented from the build plate with inclined

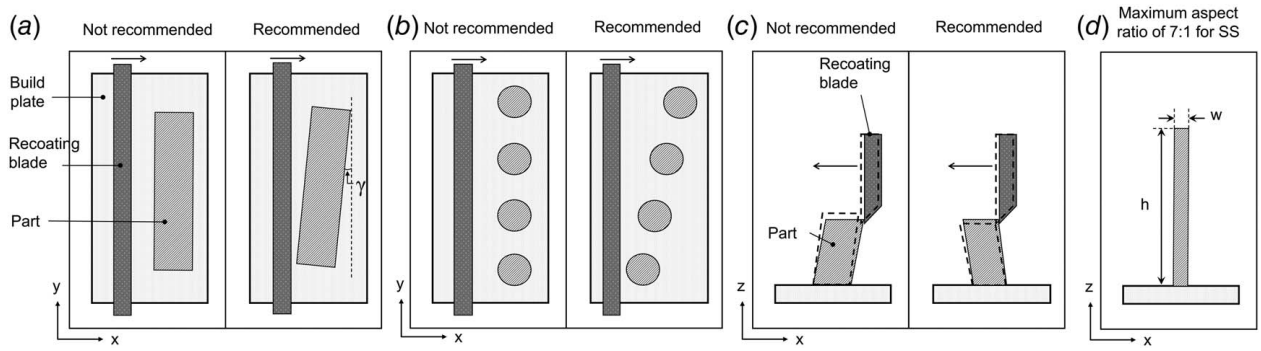

Fig. 12 (*a*) No long parallel contacts, (*b*) no multiple simultaneous contacts, (c) no deflection in upward, and (*d*) maximum aspect ratio. Reproduced from Ref. [44].

Table 7 Assumptions used for calculating the maximum HXs per build

Parameters	Symbol	Value
Work envelope size in the x-axis	L_x	250 mm
Work envelope size in the y-axis	L_y	250 mm
Work envelope size in the z-axis	L_z	325 mm
Gap between the bounding boxes in the x-axis	d_x	5 mm
Gap between the bounding boxes in the y-axis	d_y	5 mm
Distance from edge of the work envelope	d_w	5 mm
Rotation angle about the z-axis	γ	2 deg
Orientation angle	θ	45 deg
Width of full-scale HX	w	52 mm
Height of full-scale HX	h	40 mm
Length of full-scale HX	l	203 mm

angles, so the internal structures can be self-supported without the support structures.

Addressing the above guidelines in Fig. 12, this paper suggests a standardized equation for calculating the maximum number of parts per build.

$$N = \left\{\text{ROUNDDOWN}\left(\frac{L_x + d_x - 2d_w}{bb_x \cdot \cos\gamma + bb_y \cdot \sin\gamma + d_x}\right)\right\} \times \left\{\text{ROUNDDOWN}\left(\frac{L_y + d_y - 2d_w}{bb_x \cdot \sin\gamma + bb_y \cdot \cos\gamma + d_y}\right)\right\} \quad (3)$$

where L_x and L_y are the work envelope sizes in the x and y directions, d_x and d_y are the gap between the bounding box in the x and y directions, d_w is the distance between the part and the edge of a build plate, bb_x, bb_y, and bb_z are the dimensions of the bounding box in the x-, y-, and z-axis, and γ is the angle of rotation of a part about the z-axis.

The equations for calculating the dimensions of the bounding box are as follows:

$$bb_x = w \quad (4)$$

$$bb_y = l\cos\theta + h\sin\theta \quad (5)$$

$$bb_z = l\sin\theta + h\cos\theta \quad (6)$$

where w, l, and h are the width, length, and height of the part, and θ is the orientation angle.

The dimensions of 3 kW full-sized HX were used for both cost models. Also, it was assumed that the full-size HX is inclined 45 deg from the build plate so the internal channel structures are self-supported without support structures.

Using Eq. (3) and the values from Table 7, it was determined that four HXs can fit to the work envelope as shown in Fig. 13(*c*).

4.2 Hybrid Inkjet-LPBF Cycle Time. A model was used for estimating the cycle time for layering the powder, jetting the precursor ink, and scanning the laser. The equation for estimating the cycle time for depositing each powder layer (T_{layer}) is given as follows:

$$T_{\text{layer}} = \left(t_{\text{ev}} + \frac{L_x}{v_{r1}} + \frac{L_x}{v_{r2}}\right) \times (n + n_{\text{ss}}) \quad (7)$$

where t_{ev} is the time needed to elevate the build platform, v_{r1} is the positioning speed of the recoating system, v_{r2} is the powder positioning speed of the recoating system, n and n_{ss} are the number of layers for a part and a support structure, respectively. The required number of layers for a part can be calculated using Eq. (7) and the thickness of a powder layer, t.

$$n = \frac{bb_z}{t} = \frac{l\sin\theta + h\cos\theta}{t} \quad (8)$$

where t is the thickness of a powder layer.

The cycle time for laser scanning consists of the build times to rough deposit, fine deposit, and deposit the support structure.

$$T_{\text{scan}} = T_r + T_f + T_{\text{ss}} \quad (9)$$

where T_{scan} is the total scanning time per build, T_r is the rough build time, T_f is the fine build time, and T_{ss} is the build time for a support structure. Table 8 summarizes the key process parameters used in both cost models. Detailed equations can be found in prior works [45,46].

For the hybrid LPBF ODS HX model, the cycle time of jetting a precursor ink was estimated and added to times for layering powder and laser scanning to calculate a total cycle time for hybrid LPBF. The cycle time for jetting the precursor ink (T_{jet}) consists of cycle time for opening/closing the SAS door and moving the printhead per layer, and the total number of layers.

$$T_{\text{jet}} = \left(2 \times t_{\text{SAS}} + \frac{L_x}{v_p}\right) \times n \quad (10)$$

where T_{jet} is the cycle time of jetting per build, t_{SAS} is the time for extending the inkjet printhead gantry over the powder bed by opening/closing the SAS door, and v_p is the printhead speed.

The previous study [22] achieved acceptable repeatability in terms of the mass of the jetted droplets, demonstrating stable jetting performance. However, it is important to note that inkjet nozzles can become clogged, adversely affecting jetting performance. To mitigate this issue, a cleaning function was implemented

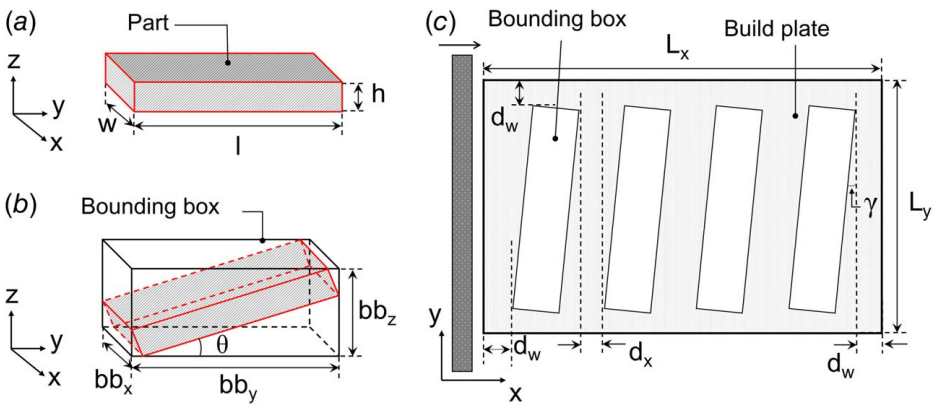

Fig. 13 (*a*) Part dimensions, (*b*) bounding box that contains the oriented part, and (*c*) positioned bounding boxes in the work envelope considering the guidelines

Table 8 Key process parameters used for both cost models

Process step	Parameter	Value
LPBF	Rough build scan speed	2000 mm/s
	Fine build scan speed	2000 mm/s
	Recoating speed	300–500 mm/s
	Layer thickness	0.040 mm
	Jetting speed (ODS 304)	200 mm/s
Heat treatment	Heating rate	5 °C/min
	Cooling rate	1.5 °C/min
	Soak temperature	817 °C (Inc625) 400 °C (ODS 304)
	Hold time at soak temperature	90 min (Inc625) 120 min (ODS 304)
Wire EDM	Material removal rate	6.710 mm^3/min
	Wire EDM kerf	0.304 mm
	Wire diameter	0.254 mm
Surface finishing	Speed	20,000 mm/min
	Width of cut	16 mm
	Infeed	0.01 mm/pass

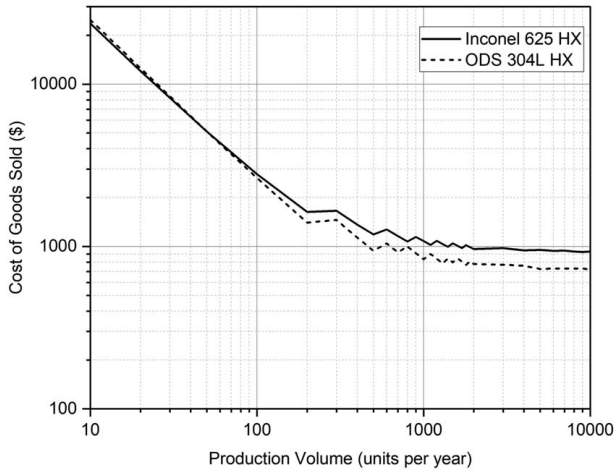

Fig. 14 Estimated unit cost as a function of annual production volume for Inconel 625 HX using LPBF and ODS 304L HX using hybrid LPBF

to clear clogged nozzles every five layers. A cleaning station was designed, constructed, and integrated inside the jetting module behind the SAS door. This station functions to wipe and clean the printhead nozzles after the ink purging process during the nozzle cleaning cycle. The inclusion of this device is crucial, as large ink droplets remaining on the orifice plate post-purging could fall onto the powder bed if not removed. Consequently, a servo code was developed to facilitate a purging cycle that involves (a) moving the printhead to the cleaning station, (b) purging ink, and (c) lowering the printhead onto the wipes at the cleaning station, thereby removing any ink residue from the orifice plate. The time spent on cleaning was not factored into the cost model, as the cleaning cycle does not impede productivity. This is because the cleaning cycle occurs within the inkjet module immediately after the jetting

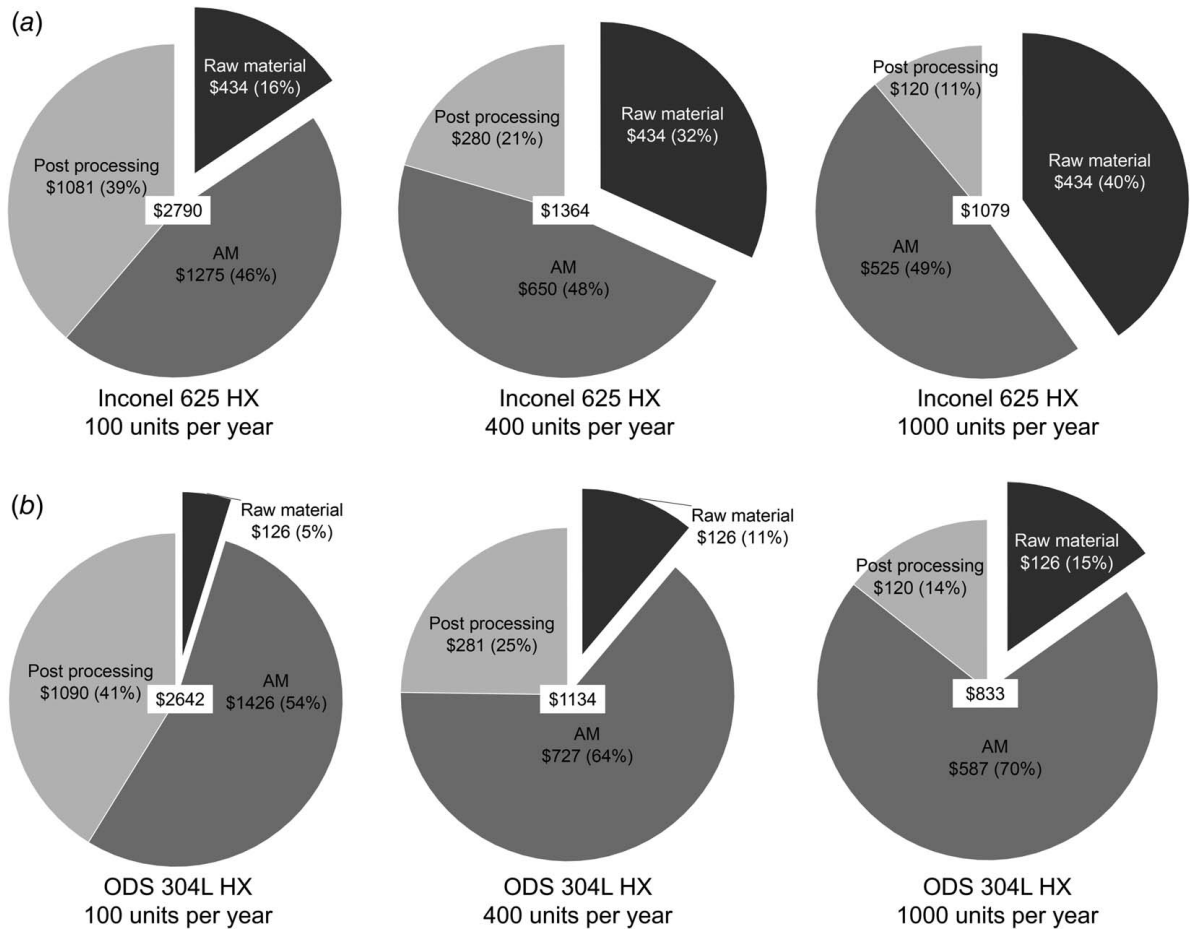

Fig. 15 A breakout of the production cost of (*a*) Inconel 625 HX and (*b*) ODS 304L HX at the production volume of 100, 400, and 1000 units per year

step is completed, ensuring that it does not disrupt other LPBF processes.

4.3 Economic Comparison. The cost of goods sold (COGS) was calculated for Inconel 625 HX produced by LPBF and ODS 304L HX produced by hybrid LPBF. The cost curve in Fig. 14 shows that the unit cost for both HXs decreases as the annual production volume increases. ODS 304L HX was slightly more expensive compared to Inconel 625 HX until the annual production volume of around 50 units per year. This is because the cost of the hybrid LPBF machine tool was assumed to be higher than the LPBF machine tool, which offsets the cost reduction because of the lower raw material cost. However, as the production volume further increases beyond 50 units per year, unit cost for ODS 304L HX is expected to cross over the one for Inconel 625 HX. At a production volume of 1000 units per year, the hybrid process is expected to allow for a reduction in the COGS from $1079 to $834. Also, the unit costs asymptotes at around $931 and $719 for Inconel 625 HX and ODS 304L HX, respectively, beyond a production volume of about 10,000 units per year.

Figure 15(*a*) shows a breakout of the unit costs of the Inconel 625 HX by process step at the production volume of 100, 400, and 1000 units per year. As the production volume increases from 100 units to 1000 units, there has been a significant increase in portion of raw material in unit cost. At the production volume of 1000 units per year, the raw material cost accounts for about 40%. However, the raw material cost of ODS 304L HX makes up only 15% at the production volume of 1000 units per year, which mainly leads to 22.8% reduction in the COGS compared to Inconel 625 HX.

5 Conclusions

The paper investigated the capabilities and economics of the hybrid inkjet-LPBF process to produce an ODS 304L SS heat exchanger. The tensile test specimens made of ODS 304L SS were produced using the hybrid inkjet-LPBF method. The tensile properties of the hybrid LPBF ODS 304L SS were measured at 600 °C and the results show that YS, UTS, and elongation of these alloy were found to be 313 ± 20 MPa, 392 ± 6 MPa, and 14 ± 1%, respectively. These YS and UTS of the hybrid LPBF ODS 304L SS at room temperature and 600 °C were similar to the values of ODS alloy produced by pre-mixing 304L SS powder with yttria nanoparticles via ball-milling, followed by LPBF. In addition, the hybrid inkjet-LPBF method for producing a microchannel heat exchanger made of ODS 304L SS was demonstrated using the LPBF machine tool modified with inkjet technology. Based on the measurements for the channel sizes, it was observed that ink doping and conversion reduced the mean channel size while increasing the standard deviation. This is because laser absorption was improved by doping the ink, which caused larger weld pools and smaller channels.

Also, the economics of hybrid LPBF method was studied by comparing the unit cost of the hybrid LPBF ODS HX with the one of LPBF Inconel 625 HX. The unit cost for ODS 304L HX is expected to be more expensive at lower production volumes, becoming less expensive than the Inconel 625 HX at higher levels of equipment utilization. Also, the hybrid process is expected to reduce the COGS from $1079 to $834 at a production volume of 1000 units per year because of the lower raw material cost. Besides, beyond a production volume of about 10,000 units per year, the unit costs are expected to asymptote at around $931 and $719 for Inconel 625 HX and ODS 304L HX, respectively, which is a reduction of about 23% compared to Inconel 625 HX.

Acknowledgment

The authors gratefully acknowledge the financial support of the National Science Foundation Advanced Manufacturing Program through Award No. 1856412. We also gratefully acknowledge the OSU Electron Microscopy Facility and the Advanced Technology and Manufacturing Institute (ATAMI) staff in particular Nick Wannenmacher.

Funding Data

- Murdock Charitable Trust (contract #2016231).
- Department of Energy (DOE) (DE-EE0007888-10-4) Advanced Manufacturing Office (AMO).
- Rapid Advancement in Process Intensification Deployment (RAPID) Institute.

Conflict of Interest

There are no conflicts of interest.

Data Availability Statement

The datasets generated and supporting the findings of this article are obtainable from the corresponding author upon reasonable request.

Nomenclature

f = friction factor
h = convective heat transfer coefficient
h = height of a part
k = thermal conductivity
l = length of a part
n = number of layers for a part
t = layer thickness
w = width of a part
A = heat transfer surface area of the heat exchanger
L = thickness of the wall
P = laser power
U = overall heat transfer coefficient
V = average velocity of the fluid
d_x = gap between the bounding box in the x-direction
d_y = gap between the bounding box in the y-direction
d_w = distance between the part and the edge of a build plate
n_{ss} = number of layers for a support structure
t_{ev} = time needed to elevate the build platform
t_{SAS} = time for extending the inkjet printhead gantry
v_{r1} = positioning speed of the recoating system
v_{r2} = powder positioning speed of the recoating system
v_p = printhead speed
A_c = flow cross-sectional area
C_R = heat capacity ratio
C_{min} = minimum heat capacity rate
C_{max} = maximum heat capacity rate
D_h = hydraulic diameter of the channel
L_{ch} = length of channels
L_x = work envelope size in the x-direction
L_y = work envelope size in the y-direction
N_{ch} = number of channels
P_w = wetted perimeter
R_{tot} = total of thermal resistance
$T_{c,i}$ = inlet temperature of the cold fluid
$T_{h,i}$ = inlet temperature of the hot fluid
$T_{c,o}$ = outlet temperature of the cold fluid
$T_{h,o}$ = outlet temperature of the hot fluid
T_{scan} = total scanning time per build
T_r = rough build time
T_{ss} = build time for a support structure
T_f = fine build time
T_{jet} = cycle time of jetting per build
hs = hatching space

Nu = Nusselt number
NTU = number of transfer units
Re = Reynolds number
bb_x = dimension of the bounding box in the x-direction
bb_y = dimension of the bounding box in the y-direction
bb_z = dimension of the bounding box in the z-direction
ε = surface roughness of the microchannel
ε = effectiveness
θ = orientation angle
μ = dynamic viscosity of the fluid
v = laser scan speed
ρ = density of the fluid
Γ = angle of rotation of a part about the z-axis
Δp = pressure drop

Appendix: Heat Exchanger Specification

A.1 Effectiveness Calculation. A theoretical effectiveness for a counter flow heat exchanger is expressed as follows:

$$\varepsilon = \frac{1 - \exp\left[-\text{NTU} \cdot (1 - C_R)\right]}{1 - C_R \cdot \exp\left[-\text{NTU} \cdot (1 - C_R)\right]} \tag{A1}$$

where ε is the effectiveness, C_R and NTU are the heat capacity ratio and the number of transfer units.

C_R and NTU can be defined as

$$C_R = \frac{C_{\min}}{C_{\max}} \tag{A2}$$

$$\text{NTU} = \frac{UA}{C_{\min}} \tag{A3}$$

where $C_{\min}$ and $C_{\max}$ are the heat capacity rates of the two fluids; and U and A are the overall heat transfer coefficient and the heat transfer surface area of the heat exchanger.

To simplify the analysis, it is assumed that the heat exchanger has a single flat channel. With the assumption of a negligible fouling factor, the overall heat transfer coefficient (U) can be expressed as

$$U = \frac{1}{R_{\text{tot}}A} = \frac{1}{\left(\frac{1}{h}\right)_{\text{tot}} + \left(\frac{L}{k}\right)_{\text{tot}}} \tag{A4}$$

where h, k, and L are convective heat transfer coefficient, thermal conductivity of the material, and thickness of the wall.

The Nusselt number (Nu) is expressed as

$$\text{Nu} = \frac{h \cdot D_h}{k} \tag{A5}$$

where D_h is the hydraulic diameter of the channel. According to Shah and London [47], the Nusselt number with constant heat flux is 8.23 for fully-developed laminar flow between flat plates.

The hydraulic diameter for a rectangular channel is

$$D_h = \frac{4 \cdot A_c}{P_w} \tag{A6}$$

where A_c and P_w are the flow cross-sectional area and the wetted perimeter, respectively.

Furthermore, the experimental effectiveness was calculated and compared to the theoretical values. It can be simplified to a temperature difference ratio as follows:

$$\varepsilon = \frac{C_c}{C_{\min}}\left(\frac{T_{c,o} - T_{c,i}}{T_{h,i} - T_{c,i}}\right) = \frac{C_h}{C_{\min}}\left(\frac{T_{h,i} - T_{h,o}}{T_{h,i} - T_{c,i}}\right) \tag{A7}$$

where $T_{c,i}$, $T_{c,o}$, $T_{h,i}$, and $T_{h,o}$ are the inlet and outlet temperatures of the cold and hot fluids, respectively.

A.2 Pressure Drop Calculation. The pressure drop through the microchannel heat exchanger was analytically calculated using Eq. (A8) for fully-developed flow.

$$\Delta p = f \times \frac{\rho \cdot V^2}{2} \times \frac{L_{\text{ch}}}{D_h} \times N_{\text{ch}} \tag{A8}$$

where f is the friction factor, ρ and V are the density and average velocity of the fluid, and L_{ch} and N_{ch} are the length and number of channels.

For the first comparison presented in Fig. 7, the friction factor, which is dependent on the Reynolds number (Re) for fully-developed laminar flow, can be calculated using Eq. (A9) from Shah and London [47].

$$f = \frac{64}{\text{Re}} \tag{A9}$$

The Reynolds number is expressed as follows:

$$\text{Re} = \frac{\rho \cdot V \cdot D_h}{\mu} \tag{A10}$$

where μ is the dynamic viscosity of the fluid.

In the second comparison shown in Fig. 8, Eq. (A11), known as the von Karman equation, was employed to determine the friction factor for the fully-developed turbulent flow regime in a rough microchannel [48]

$$\left(\frac{1}{f}\right)^{0.5} = 2\log\left(\frac{3.7}{\varepsilon/D_h}\right) \tag{A11}$$

where ε is the surface roughness of the microchannel.

References

[1] Dincer, I., and Acar, C., 2015, "Review and Evaluation of Hydrogen Production Methods for Better Sustainability," Int. J. Hydrogen Energy, **40**(34), pp. 11094–11111.
[2] Zheng, R., Diver, R., Caldwell, D., Fritz, B., Cameron, R., Humble, P., TeGrotenhuis, W., Dagle, R., and Wegeng, R., 2015, "Integrated Solar Thermochemical Reaction System for Steam Methane Reforming," Energy Procedia, **69**, pp. 1192–1200.
[3] Brannon, S. T., and Paul, B. K., 2015, "The Development of Drawn Microchannel Flow Inserts for High Temperature Waste Heat Recuperators," International Manufacturing Science and Engineering Conference, American Society of Mechanical Engineers, p. V001T002A076.
[4] Paul, B. K., 2006, "Micro Energy and Chemical Systems (MECS) and Multiscale Fabrication," *Micromanufacturing and Nanotechnology*, N. P. Mahalik, ed., Springer, Berlin, Heidelberg, pp. 299–355.
[5] Kelly, J., 2019, "Low-Cost Recuperative Heat Exchanger for Supercritical Carbon Dioxide Power Systems, Final Scientific/Technical Report," Altex Technologies Corporation.
[6] Hirata, A., Fujita, T., Wen, Y., Schneibel, J., Liu, C. T., and Chen, M., 2011, "Atomic Structure of Nanoclusters in Oxide-Dispersion-Strengthened Steels," Nat. Mater., **10**(12), pp. 922–926.
[7] Alamo, A., Regle, H., Pons, G., and Béchade, J. L., 1992, "Microstructure and Textures of ODS Ferritic Alloys Obtained by Mechanical Alloying," Mater. Sci. Forum, **88–90**, pp. 183–190.
[8] Odette, G. R., Cunningham, N. J., Stan, T., Alam, M. E., and De Carlan, Y., 2019, "Nano-Oxide Dispersion-Strengthened Steels," *Structural Alloys for Nuclear Energy Applications*, G. R. Odette and S. J. Zinkle, eds., Elsevier, New York, pp. 529–583.
[9] Zhang, C., and Gümmer, V., 2019, "High Temperature Heat Exchangers for Recuperated Rotorcraft Powerplants," Appl. Therm. Eng., **154**, pp. 548–561.
[10] Maier, B., Lenling, M., Yeom, H., Johnson, G., Maloy, S., and Sridharan, K., 2019, "A Novel Approach for Manufacturing Oxide Dispersion Strengthened (ODS) Steel Cladding Tubes Using Cold Spray Technology," Nucl. Eng. Technol., **51**(4), pp. 1069–1074.
[11] Yang, S., 2023, "Additive Manufacturing of Austenitic Oxide Dispersion Strengthened Alloy Using Powder Feedstock Gas-Atomized With Elemental Yttrium Via Laser Directed Energy Deposition," Masters thesis, Oregon State University, Corvallis, OR.
[12] Wilms, M. B., Pirch, N., and Gökce, B., 2023, "Manufacturing Oxide-Dispersion-Strengthened Steels Using the Advanced Directed Energy Deposition Process of High-Speed Laser Cladding," Prog. Addit. Manuf., **8**(2), pp. 159–167.
[13] Gibson, I., Rosen, D. W., and Stucker, B., 2014, *Additive Manufacturing Technologies*, Springer, New York.

[14] Zhao, C., Fezzaa, K., Cunningham, R. W., Wen, H., De Carlo, F., Chen, L., Rollett, A. D., and Sun, T., 2017, "Real-Time Monitoring of Laser Powder Bed Fusion Process Using High-Speed X-ray Imaging and Diffraction," Sci. Rep., **7**(1), p. 3602.
[15] Grasso, M., and Colosimo, B. M., 2017, "Process Defects and In Situ Monitoring Methods in Metal Powder Bed Fusion: A Review," Meas. Sci. Technol., **28**(4), p. 044005.
[16] Paul, B. K., O'Connor, J. T., and Haapala, K. R., 2021, "Managing Business Risk in Modular Chemical Process Intensification," Chem. Eng. Prog., **117**(3), pp. 22–27.
[17] Kenel, C., Dawson, K., Barras, J., Hauser, C., Dasargyri, G., Bauer, T., Colella, A., et al., 2017, "Microstructure and Oxide Particle Stability in a Novel ODS γ-TiAl Alloy Processed by Spark Plasma Sintering and Laser Additive Manufacturing," Intermetallics, **90**, pp. 63–73.
[18] Bourell, D., Kruth, J. P., Leu, M., Levy, G., Rosen, D., Beese, A. M., and Clare, A., 2017, "Materials for Additive Manufacturing," CIRP Ann., **66**(2), pp. 659–681.
[19] Ghayoor, M., Lee, K., He, Y., Chang, C.-H., Paul, B. K., and Pasebani, S., 2020, "Selective Laser Melting of Austenitic Oxide Dispersion Strengthened Steel: Processing, Microstructural Evolution and Strengthening Mechanisms," Mater. Sci. Eng. A, **788**, p. 139532.
[20] Ghayoor, M., Mirzababaei, S., Sittiho, A., Charit, I., Paul, B. K., and Pasebani, S., 2021, "Thermal Stability of Additively Manufactured Austenitic 304L ODS Alloy," J. Mater. Sci. Technol., **83**, pp. 208–218.
[21] Horn, T., Rock, C., Kaoumi, D., Anderson, I., White, E., Prost, T., Rieken, J., Saptarshi, S., Schoell, R., and DeJong, M., 2022, "Laser Powder Bed Fusion Additive Manufacturing of Oxide Dispersion Strengthened Steel Using Gas Atomized Reaction Synthesis Powder," Mater. Des., **216**, p. 110574.
[22] Paul, B. K., Lee, K., He, Y., Ghayoor, M., Chang, C.-H., and Pasebani, S., 2020, "Oxide Dispersion Strengthened 304 L Stainless Steel Produced by Ink Jetting and Laser Powder Bed Fusion," CIRP Ann., **69**(1), pp. 193–196.
[23] Pasebani, S., Baghbani, S. M. G., Paul, B. K., Chang, C.-H., Lee, K., and Yujuan, H., 2021, "Additive-Containing Alloy Embodiments and Methods of Making and Using the Same," Google Patents.
[24] Ghayoor, M., Sadeghi, O., Cox, B., Gess, J., and Pasebani, S., 2023, "On the Melt Pool Dynamic of Voxel-Controlled Metal Matrix Composites Via Hybrid Additive Manufacturing: Laser Powder Bed Fusion and Ink-Jetting," J. Manuf. Process., **89**, pp. 314–327.
[25] Lee, K., Doddapaneni, V. V. K., Mirzababaei, S., Pasebani, S., Chang, C.-H., and Paul, B. K., 2022, "Synthesis of a 316L Stainless Steel–Copper Composite by Laser Melting," Addit. Manuf. Lett., **3**, p. 100058.
[26] Mirzababaei, S., Doddapaneni, V. V. K., Lee, K., Paul, G. E., Pirgazi, H., Tan, K.-S., Ertorer, O., Chang, C.-H., Paul, B. K., and Pasebani, S., 2023, "Remarkable Enhancement in Thermal Conductivity of Stainless-Steel Leveraging Metal Composite Laser Powder Bed Fusion: 316L-Cu Composite," Addit. Manuf., **70**, p. 103576.
[27] Melnikov, P., Nascimento, V., Consolo, L., and Silva, A., 2013, "Mechanism of Thermal Decomposition of Yttrium Nitrate Hexahydrate, Y (NO3)3·6H2O and Modeling of Intermediate Oxynitrates," J. Therm. Anal. Calorim., **111**(1), pp. 115–119.
[28] Iron, A., 1979, *High-Temperature Characteristics of Stainless Steels, Committee of Stainless Steel Producers*, Toronto, Ontario, Canada.
[29] Xu, Y., Zhou, Z., Li, M., and He, P., 2011, "Fabrication and Characterization of ODS Austenitic Steels," J. Nucl. Mater., **417**(1–3), pp. 283–285.
[30] Wang, M., Zhou, Z., Sun, H., Hu, H., and Li, S., 2013, "Microstructural Observation and Tensile Properties of ODS-304 Austenitic Steel," Mater. Sci. Eng. A, **559**, pp. 287–292.
[31] Shi, Y., Lu, Z., Xu, H., Xie, R., Ren, Y., and Yang, G., 2019, "Microstructure Characterization and Mechanical Properties of Laser Additive Manufactured Oxide Dispersion Strengthened Fe-9Cr Alloy," J. Alloys Compd., **791**, pp. 121–133.
[32] Lee, J., Terner, M., Jun, S., Hong, H.-U., Copin, E., and Lours, P., 2020, "Heat Treatments Design for Superior High-Temperature Tensile Properties of Alloy 625 Produced by Selective Laser Melting," Mater. Sci. Eng. A, **790**, p. 139720.
[33] Kim, K.-S., Kang, T.-H., Kassner, M. E., Son, K.-T., and Lee, K.-A., 2020, "High-Temperature Tensile and High Cycle Fatigue Properties of Inconel 625 Alloy Manufactured by Laser Powder Bed Fusion," Addit. Manuf., **35**, p. 101377.
[34] Ma, S., and Wang, X., 2019, "Mechanical Properties and Fracture of In-Situ Al3Ti Particulate Reinforced A356 Composites," Mater. Sci. Eng. A, **754**, pp. 46–56.
[35] Sun, Y., Zhao, Y., Wu, J., Kai, X., Zhang, Z., Fang, Z., and Xia, C., 2020, "Effects of Particulate Agglomerated Degree on Deformation Behaviors and Mechanical Properties of In-Situ ZrB2 Nanoparticles Reinforced AA6016 Matrix Composites by Finite Element Modeling," Mater. Res. Express, **7**(3), p. 036507.
[36] Mala, G. M., and Li, D., 1999, "Flow Characteristics of Water in Microtubes," Int. J. Heat Fluid Flow, **20**(2), pp. 142–148.
[37] Brkić, D., and Praks, P., 2018, "Unified Friction Formulation From Laminar to Fully Rough Turbulent Flow," Appl. Sci., **8**(11), p. 2036.
[38] Perachon, G., Thourey, J., and Mathurin, D., 1977, "Formation Enthalpies of Hexahydrated Yttrium Nitrate and the Y 3+-ion," Thermochim. Acta, **18**(2), pp. 229–234.
[39] Robie, R. A., and Hemingway, B. S., 1995, *Thermodynamic Properties of Minerals and Related Substances at 298.15 K and 1 bar (105 Pascals) Pressure and at Higher Temperatures*, US Government Printing Office, Washington, DC.
[40] Chase, M. W. Jr, 1998, "NIST-JANAF Thermochemical Tables," J. Phys. Chem. Ref. Data, **9**.
[41] Gao, Q., Lizarazo-Adarme, J., Paul, B. K., and Haapala, K. R., 2016, "An Economic and Environmental Assessment Model for Microchannel Device Manufacturing: Part 1–Methodology," J. Cleaner Prod., **120**, pp. 135–145.
[42] Paul, B. K., McNeff, P., Brannon, S., and O'Halloran, M., 2019, "The Role of Manufacturing Process Design in Technology Commercialization," *Emerging Frontiers in Industrial and Systems Engineering: Success Through Collaboration*, Taylor & Francis Group, pp. 259–288.
[43] Yim, S., and Rosen, D., 2013, "Build Time and Cost Models for Additive Manufacturing Process Selection," ASME 2012 International Design Engineering Technical Conferences and Computers and Information in Engineering Conference, Chicago, IL, Aug. 12–15, American Society of Mechanical Engineers Digital Collection, pp. 375–382.
[44] Moylan, S. P., Slotwinski, J. A., Cooke, A., Jurrens, K., and Donmez, M. A., 2013, "Lessons Learned in Establishing the NIST Metal Additive Manufacturing Laboratory," NIST Technical Note.
[45] Pham, D. T., and Wang, X., 2000, "Prediction and Reduction of Build Times for the Selective Laser Sintering Process," Proc. Inst. Mech. Eng., Part B, **214**(6), pp. 425–430.
[46] Manoharan, S., Lee, K., Freiberg, L., Coblyn, M., Jovanovic, G., and Paul, B. K., 2019, "Comparing the Economics of Metal Additive Manufacturing Processes for Micro-Scale Plate Reactors in the Chemical Process Industry," Procedia Manuf., **34**, pp. 603–612.
[47] Shah, R. K., and London, A. L., 2014, *Laminar Flow Forced Convection in Ducts: A Source Book for Compact Heat Exchanger Analytical Data*, Academic Press, Cambridge, MA.
[48] Dzarma, G., Adeyemi, A., and Taj-Liad, A., 2020, "Effect of Inner Surface Roughness on Pressure Drop in a Small Diameter Pipe," Int. J. Novel Res. Eng. Pharm. Sci., **7**(1), pp. 1–8.